

Local Stability Enhancement of Immersed Boundary Methods

Christoph Brehm*, and Hermann F. Fasel**

Corresponding author: christoph.brehm@nasa.gov

* Science and Technology Corporation, Moffett Field, CA, USA.

** University of Arizona, AZ, USA.

Abstract: The objective of this work is to develop a strategy to improve the robustness of immersed boundary methods. The basic approach was introduced for specific types of partial differential equations in our previous publications. This paper elaborates on these ideas and provides a more general framework on how to apply the concept of local stability enhancement to different types of problems of engineering interest. The key feature of this immersed boundary method is that local stability constraints are taken into account in the derivation of the finite-difference stencil coefficients at irregular grid points. Various applications of this immersed method are presented to incorporate high-order discretization and fluid-structure-interaction problems, where numerical robustness is still a key issue. The variety of successful applications of this immersed boundary approach demonstrates the robustness and flexibility of the method achieved through improved stability characteristics.

Keywords: Immersed Boundary, Immersed Interface, Numerical Stability Analysis.

1 Introduction and Motivation

One of the principal goals of current Computational Fluid Dynamics (*CFD*) is the development of numerical algorithms that can deliver computationally efficient and highly accurate solutions for a wide range of applications involving multi-physics problems, e.g. Fluid Structure Interaction (*FSI*). For simulations with highly complex geometries, which are frequently encountered in many fields of science and engineering, the process of generating a high-quality, body-fitted grid is complicated and time-intensive. Immersed boundary methods, which can overcome some of these difficulties, provide considerable advantages over conventional approaches, especially for flow problems containing moving boundaries or interfaces.

Immersed Boundary (*IB*) methods have been around for several decades and have appeared in various forms since they were first introduced in the 1970s [31]. These methods have become increasingly relevant and are considered valuable for numerically solving initial boundary-value problems on domains with complex geometries. One considerable advantage of these methods is their simplicity in obtaining grids, independent of the complexity of the geometry. The grid generation process for body-conformal structured or unstructured grids is generally cumbersome, because the grid generation process aims at generating a grid that offers sufficient local resolution without exceeding a maximum number of total grid points. For anything but the simplest geometries, these conflicting requirements can lead to deterioration in grid quality, thereby negatively impacting the accuracy and convergence properties of the solver (Ferziger and Peric [18]). For simulating flows with moving or deforming boundaries, the use of body-conformal grids requires generating a new grid at each time-step in addition to a procedure capable of projecting the solution onto this new grid (Tezduyar [39]). These two requirements associated with simulating flows with moving boundaries may negatively impact the accuracy, robustness, and computational cost for such applications. As a result, immersed boundary methods are a promising alternative to body-fitted grid approaches. For flows containing moving boundaries, immersed interface/boundary methods provide clear advantages over conventional approaches (e.g. Arbitrary Lagrangian-Eulerian (*ALE*) approach). They provide a convenient numerical technique that allows the body to move or deform on a stationary non-deforming Cartesian grid. While these methods simplify the grid generation process, a detailed mathematical understanding of the immersed boundary method

is necessary to avoid a negative impact of the boundary treatment on the convergence behavior, stability properties and the accuracy of the numerical scheme.

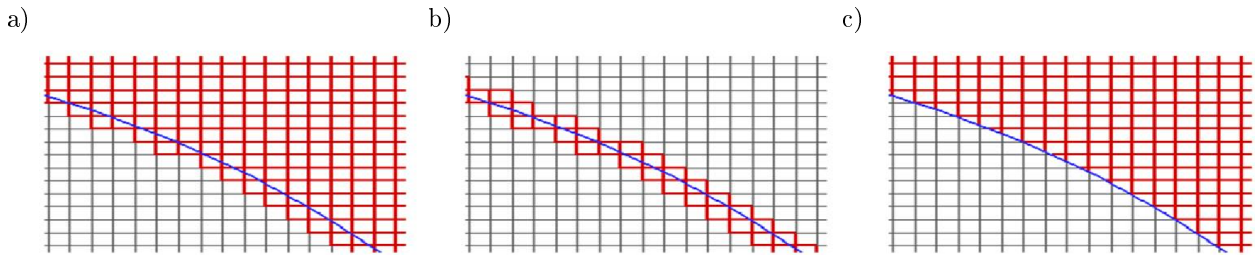


Figure 1: Rough classification of immersed boundary methods: (a) Stair-step approach, (b) classical immersed boundary approach, and (c) sharp-boundary method.

Immersed boundary methods can be classified into roughly three groups as displayed in Figure 1. In this categorization, the word “boundary” may be used interchangeably with the word “interface”. Within the scope of this paper it is assumed that a boundary separates the solid domain from the fluid domain and an interface separates two different materials, which have different material properties, such as density, viscosity, etc. For the “stair-step approach” shown in Figure 1a, the geometry is approximated by a stair-step pattern. In this approach, a grid point, which is located in the vicinity of the immersed boundary, is considered to be inside or outside of the computational domain depending on its actual position with respect to the boundary or interface. The “stair-step approach” can be easily implemented in any existing solver without any extensive modification of the underlying source code. Its simplicity, however, is accompanied with a few obvious disadvantages. For example, the approach is only first-order accurate in the vicinity of the boundary. Also for moving boundary problems, the immersed boundary jumps from one discrete grid point (in the vicinity of the immersed boundary) to the next; therefore, no continuous boundary motion can be captured with this approach.

The second group of schemes, schematically shown in Figure 1b, is here referred to as the “classical immersed boundary approach”. The pioneering immersed boundary method by Peskin [34, 35] falls into this category. In this approach, the governing equations are modified at cells (in a finite-volume sense) cut by the boundary by adding a source term on the right-hand-side of the equations. The boundary conditions in this approach are indirectly enforced by the forcing function, which causes the numerical solution to fulfill the prescribed boundary conditions. These methods provide usually lower-order accuracy in the vicinity of the boundary. Since in general the immersed boundary does not coincide with the discrete grid points, the forcing term needs to be applied over several grid points in the vicinity of the boundary, which causes a smearing effect near the boundary.

The last group of immersed schemes, shown in Figure 1c, is called the “sharp-boundary method”. The key feature of this approach is that computational stencils are modified such that the information on the boundary is used exactly where grid lines intersect the immersed boundary. In this approach, the governing equations are first discretized and then the boundary conditions are enforced directly by the modification of the grid stencil. The representation of the immersed boundary as a sharp boundary (as its name implies) is highly desirable for transition research where the near wall accuracy is critically important to accurately predict the stability characteristics of wall-bounded flows. We chose to develop a method which falls into the last category. With this method, we are targeting applications in the field of transition research involving stability analysis investigations and/or DNS (or DNS like) studies.

Due to current inefficiencies of immersed methods for resolving boundary layers in high Reynolds number flows, the scope of applications for immersed boundary methods are currently limited to low Reynolds number applications. Such applications include biological flows, such as blood flow (Figure 2a), and flow scenarios where the inviscid flow assumption can be justified, such as launch environment flows (see for example Moini-Yekta *et al.* [32]) provided the pressure signature is the primary focus of the analysis (Figure 2b).

The current paper is organized as follows: First, the basic concept of local stability enhancement of immersed boundary methods is introduced; second, the local stability enhancement strategy is derived for a sample problem (here, the 1-D advection-diffusion equation); in last part of the paper, the local stability

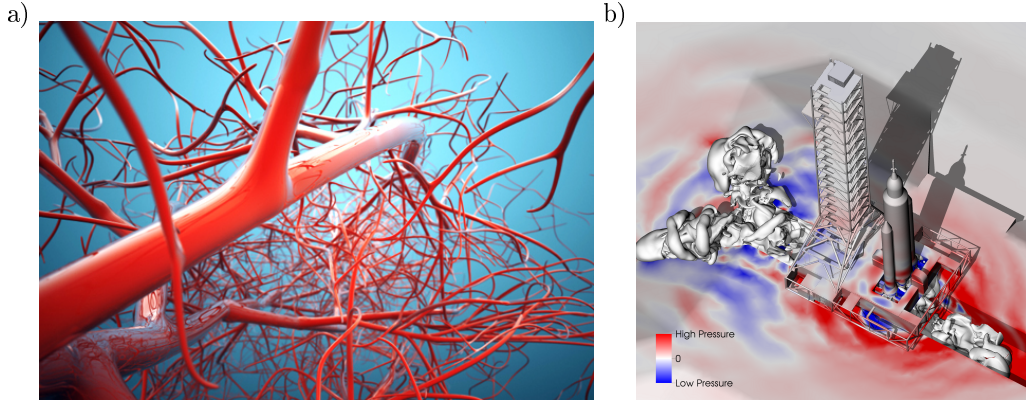


Figure 2: (a) Schematic illustrating the complexity of the artery tree in the human body (taken from iStockphoto). (b) Numerical Simulation of launch environment for a heavy-lift vehicle displaying colored pressure contours and iso-surface of total temperature (taken from Moini-Yekta *et al.* [32]).

enhancement strategy is applied to various types of equations, including the Poisson equation, incompressible and compressible Navier-Stokes equations, and Maxwell's equations.

1.1 Basic Concept of Local Stability Enhancement

This paper presents a strategy on how to locally improve the stability characteristics of immersed boundary methods. Many immersed methods have been developed in the past; however, in the derivation of these schemes usually only the order of the local truncation error or accuracy of the numerical scheme has been considered. *A posteriori*, the numerical stability of these schemes is commonly demonstrated (in a global sense) by considering a number of different test-problems, and in a few cases, an additional global matrix stability analysis is employed (see for example Zhong [47]). Stability and convergence characteristics are essential in developing immersed boundary methods for high-order schemes and/or fluid-structure-interaction. This paper will demonstrate that local stability constraints can be derived to improve the spectral properties of the finite-difference stencils at grid points with irregular stencils. The basic concept is not limited to finite-difference methods and can also be applied to finite-volume or even finite-element schemes. These extensions, however, are beyond the scope of this paper and will be part of follow-up publications.

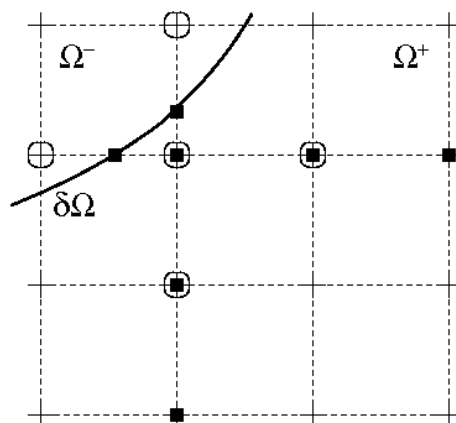


Figure 3: Schematic of a finite-difference stencil at an irregular grid point (marked by ■) and an idealized/interior finite-difference stencil at the same grid point (marked by ○). The immersed boundary, $\delta\Omega$, separates the fluid domain, Ω^+ , from the solid domain, Ω^- .

The notion of developing a strategy for improving the spectral properties of immersed methods originated

from the idea that the stability of the numerical scheme can be formulated as an N -dimensional optimization problem, where N represents the number of irregular grid points. In this paper, an irregular grid point is present when a regular (interior) grid stencil crosses the computational (fluid/solid) boundary or an interface separating two regions with different material properties (see Figure 3). Instead of solely considering the local truncation error in the derivation of the finite-difference grid stencil at an irregular grid point, an over-determined system of equations is constructed to determine the stencil coefficients. We employed an over-determined system of equations because it allows for selection of free parameters, which can be tuned towards optimizing the local stability properties of the finite-difference stencil. Assuming one free parameter per irregular grid point we obtained an N -dimensional optimization problem for N irregular grid points.

The objective function of the optimization problem must be customized depending on the nature of the particular partial-differential equation of interest. For advection-diffusion-type equations, the spectral radius of the update matrix may be considered as an objective function. In the current paper, we refer to the update matrix as the matrix which updates the solution from time t_n to next time-step, t_{n+1} . The update matrix, therefore, contains the spatial and temporal discretization of the numerical scheme. The spectral radius is well-suited in this situation, because its actual value is associated with the stability of the numerical scheme and it can be used to formulate a necessary condition for stability of the update matrix. For non-linear systems of equations, a linearization is necessary prior to applying the outlined linear stability analysis concepts. Note that this paper is exclusively concerned with the linear stability of the immersed boundary scheme and therefore neglects possible non-linear effects on the stability.

For elliptic equations, the objective function can be based on the local discrete maximum principle, as previously discussed by various researchers, e.g. Ciarlet [14], Guy and Fogelson [20], etc. Using this procedure, the desired M-matrix can be achieved. Applying the local discrete maximum principle ensures that the global discretization matrix sustains the spectral properties of the interior scheme. Hence, the basic concept of local stability/convergence enhancement, which aims at optimizing the spectral properties of the numerical scheme by fine-tuning the irregular stencil coefficients, can also be applied to elliptical equations.

2 Local Stability Enhancement for a Sample Problem

This paper discusses various extensions of the particular immersed boundary method initially introduced by Brehm and Fasel [3]. In this section, it will be demonstrated that it is possible to not only consider the local truncation error or accuracy of the numerical scheme at irregular grid points but it is also possible to include the local stability of the scheme in the derivation of the finite-difference stencil coefficients. The objective of the present method is to improve the robustness of the immersed boundary method without compromising accuracy. To achieve this objective when solving a coupled partial differential equation (in space and time), it is important to incorporate the actual coupling between the temporal and spatial operator in a discrete sense. When simply considering the stability properties of the spatial operator, the finite-difference stencil coefficients can only be constrained by necessary conditions. These conditions may apply a much weaker constraint on the choice of the stencil coefficients than if one would base it on a necessary and/or sufficient condition of stability including the spatial and temporal coupling.

As stated in the introduction, we are seeking to solve an optimization problem with respect to the stability of the numerical scheme. In a global sense, one free parameter may be chosen per finite-difference stencil at irregular grid points, which leads to an N -dimensional optimization problem for N irregular grid points. In principal, it is possible to solve such a large system of equations. From a practical point of view, however, it is not very efficient or desirable to solve such a large system of equations, especially for FSI problems where the grid topology is time dependent, thereby requiring this procedure to be repeated at each time-step. Therefore, in the current approach, we aimed at isolating the boundary stencils from the remainder of the computational domain so that the optimization problem can be formulated for each irregular grid-point separately. Instead of solving a global N -dimensional optimization problem we solved N one-dimensional optimization problems at each irregular grid point individually. This approach greatly reduces the computational effort needed to determine the “optimal” stencil coefficients. We refer to the aspect of turning the global N -dimensional problem into N one-dimensional problems as “localization” or “localization assumption”. In Brehm and Fasel [3], it was demonstrated, both numerically and analytically, that for advection-diffusion type equations, the localization assumption appears to be valid as long as the

diffusion number does not reach a limiting value. In the following discussion, the basic steps for deriving the immersed boundary method are briefly outlined. Note that the following discussion does not provide a detailed derivation or explanation of the current immersed boundary method, it merely intends to provide an overview of the main ideas. For a more detailed discussion, the interested reader is referred to Brehm and Fasel [3, 4].

A simple 1-D advection-diffusion equation,

$$\frac{\partial \phi}{\partial t} = -c_x \frac{\partial \phi}{\partial x} + \frac{\partial}{\partial x} \left(\beta \frac{\partial \phi}{\partial x} \right), \quad (1)$$

is taken as a sample problem to outline the main steps of the approach. In Equation 1, c_x is the advection speed and β is the diffusion coefficient. In the following discussion, Equation 1 is discretized over a compu-

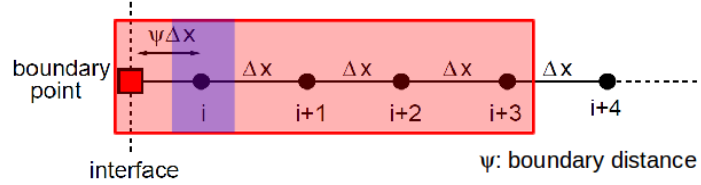


Figure 4: Finite-difference stencil at an irregular grid point, x_i , including a boundary point (marked as a \square) and three additional neighboring grid points (red-shaded region).

tational domain of unit length as shown in Figure 4. An irregular grid point is assumed at the left end of the computational domain with a boundary distance of $\psi \Delta x$ to the neighboring grid point, x_i .

The finite-difference stencil coefficients are derived by following the three steps listed below:

1. The first step in the derivation of the stencil coefficients is the common Taylor series procedure for determining the discretization coefficients of finite-difference schemes. To achieve a desired order-of-accuracy of the finite-difference stencil at an irregular grid-point, the continuous advection-diffusion operator is balanced against its discrete approximation. The truncation error for the convection-diffusion operator, a model for the momentum equation of the Navier-Stokes equation, is given here as an example:

$$\begin{aligned} \tau_i = & \left(-c_x \frac{\partial u}{\partial x} + \frac{\partial}{\partial x} \left(\beta \frac{\partial u}{\partial x} \right) + f \right)_{x=x_i} \\ & - (\hat{u}_B \alpha_1 + \hat{u}_i \alpha_2 + \hat{u}_{i+1} \alpha_3 + \hat{u}_{i+2} \alpha_4 + \hat{u}_{i+3} \alpha_5 + C), \end{aligned} \quad (2)$$

where the variables α_k represent the stencil coefficients, C is an additional constant absorbing the source term, $f(x_i)$, and \hat{u}_i is the discrete approximation of the continuous quantity, u . In order to achieve second-order accuracy, only four stencil coefficients are needed. However, to provide improved stability characteristics of the immersed boundary scheme, an additional grid point is added and used as a free parameter to fine-tune the finite-difference stencil in the vicinity of the boundary with respect to numerical stability.

2. One of the key features of this immersed boundary approach is the consideration of local constraints in order to stabilize the numerical method. In this derivation, the spatial discretization represented by $\underline{\mathbf{A}}$ is coupled with the temporal discretization to form the combined temporal and spatial discretization matrix, $\underline{\mathbf{A}}$. A simple Euler-forward time-integration is applied, leading to the combined temporal and spatial discretization matrix,

$$\underline{\mathbf{A}} = \underline{\mathbf{I}} + \Delta t \tilde{\underline{\mathbf{A}}}. \quad (3)$$

Formally, the combined temporal and spatial discretization matrix, $\underline{\mathbf{A}}$, can be written as a product of two matrices

$$\underline{\mathbf{A}} = \underline{\mathbf{E}} \cdot \underline{\mathbf{A}}_{id}. \quad (4)$$

Since the two matrices, $\underline{\mathbf{A}}$ and $\underline{\mathbf{A}}_{id}$, only differ in the first row, due to the different coefficients at the irregular boundary stencil, it is straightforward to notice that the matrix, $\underline{\mathbf{E}}$, embodies an extremely simple form. The matrices, $\underline{\mathbf{A}}$ and $\underline{\mathbf{E}}$, used for the 1-D sample case are shown below.

$$\underline{\mathbf{E}} = \begin{pmatrix} a & b & c & d & e & \dots \\ 0 & 1 & 0 & 0 & 0 & \dots \\ 0 & 0 & 1 & 0 & 0 & \dots \\ \vdots & \vdots & \vdots & \vdots & \vdots & \ddots \end{pmatrix} \quad \text{and} \quad \underline{\mathbf{A}} = \begin{pmatrix} 1 + \Delta t \alpha_2 & \Delta t \alpha_3 & \Delta t \alpha_4 & \Delta t \alpha_5 & 0 & \dots \\ * & * & * & * & * & \dots \\ * & * & * & * & * & \dots \\ \vdots & \vdots & \vdots & \vdots & \vdots & \ddots \end{pmatrix} \quad (5)$$

The purpose of matrix $\underline{\mathbf{E}}$ is to project matrix $\underline{\mathbf{A}}_{id}$ onto the combined temporal and spatial discretization matrix, $\underline{\mathbf{A}}$. Matrix $\underline{\mathbf{E}}$ essentially isolates the effect of the irregular grid point on the global discretization. In this context, $\underline{\mathbf{A}}_{id}$ represents the full discretization matrix on a grid without an immersed boundary ($\psi_x = \psi_y = 1$ in Figure 3). The fifth stencil coefficient (for the second-order scheme) is determined by including a local stability constraint. This constraint can be formulated in terms of a necessary condition for the stability of the combined temporal and spatial discretization matrix employing the spectral radius or the local stability constraint can be based on a sufficient condition for the stability employing a consistent matrix norm. For the remainder of this paper it is assumed that the free parameter of the over-determined system of equations is found by minimizing the L_2 -norm of the perturbation matrix, $\underline{\mathbf{E}}$.

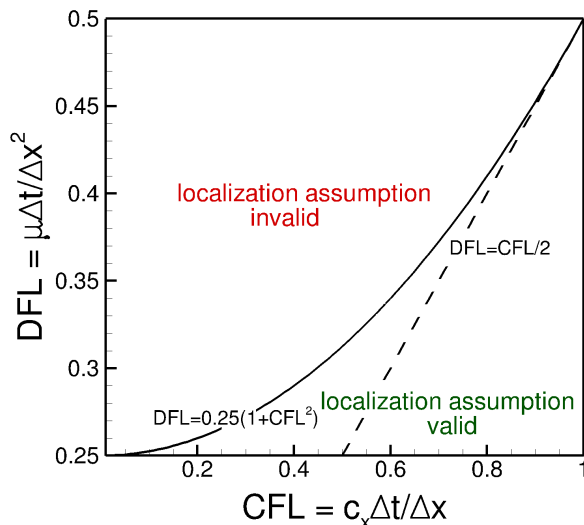


Figure 5: Regions where the localization assumption valid and invalid. The diffusion number, here also referred to as DFL -number, is defined as $\mu \Delta t / \Delta x^2$ and the Courant-Friedrichs-Levy number, CFL -number, is defined as $c_x \Delta t / \Delta x$.

3. In the last step of the derivation of the immersed scheme, it must be demonstrated that for strongly convective problems, the stability of the discretization matrix can be determined locally. As previously stated, we are solving N one-dimensional optimization problems instead of one N -dimensional optimization problem. Hence, it is essential that the irregular grid stencils can be isolated from the rest of the computational domain so that their stability behavior can be adjusted locally. The validity of the localization assumption was demonstrated both numerically and analytically in Brehm and Fasel [4, 3]. The diagram shown in Figure 5 is based on an analytical examination of the localization assumption and displays the regions where it is valid and invalid. The localization assumption can be justified as long as the diffusion number does not exceed an upper limit shown here as a solid black line. Note that the results shown in Figure 5 are based on a particular advection-diffusion-type equation, and therefore, the findings must be carefully applied to other types of equations. For more details regarding

the derivation of the current immersed scheme see Brehm *et al.* [3, 4, 7, 9].

3 Extensions of the Immersed Method

In this section, we will outline several extensions of the immersed boundary method, which was introduced in the previous section. The intention here is to merely provide an overview on how to extend the local stability enhancement approach to more complicated problems. It will be demonstrated that the idea of locally adjusting the grid stencil in order to closely mimic the spectral characteristics of an "ideal scheme" is applicable to a wide variety of equations. Depending on the type of equations, e.g. hyperbolic or elliptic, a different closure of the over-determined system of equations may be necessary, e.g. locally enforcing the discrete maximum principle for elliptical equations, preserving continuity or an energy norm for interpolation operators, etc.

3.1 Elliptic Equations

The immersed boundary method for elliptic equations was designed within the context of developing a new Incompressible Navier-Stokes (INS) solver. To numerically solve the incompressible Navier-Stokes equations, the approximate projection method is employed as a fractional-step method type approach (see Kim and Moin [24], Rai and Moin [36], and Brown *et al.* [13]). The basic goal of the projection method is to first advance the velocity field by disregarding the solenoidal nature of the velocity. Then the desired divergence-free vector field is recovered by solving for a correction term, which will be added to the intermediate velocity field in order to ensure the solenoidal nature of the velocity field. In the second step of the fractional-step method, the so-called pressure correction, ϕ^{n+1} , is computed by solving a Poisson equation,

$$\nabla^2 \phi^{n+1} = \frac{\nabla \cdot \mathbf{u}}{\Delta t}, \quad (6)$$

with Neumann boundary condition, $\mathbf{n} \cdot \nabla \phi |_{\partial\Omega} = 0$.

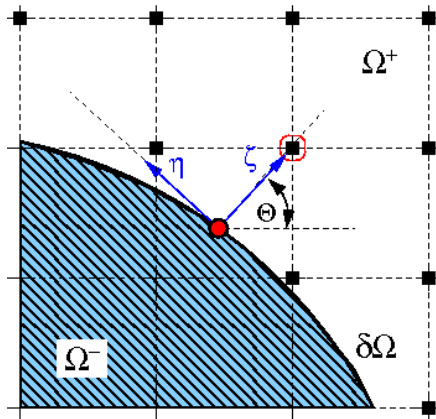


Figure 6: Local coordinate system at irregular grid point $x_{i,j}$.

The Laplace operator acting on the pressure correction field, ϕ , represents one of the main pieces of the immersed INS solver. Considering that the vast majority of the computational effort needed to solve the incompressible Navier-Stokes equations is spent solving the Poisson equation, it is evident that this part of the entire INS solver must be computationally efficient. The immersed boundary approach used to determine the coefficients of the Laplace stencil at an irregular grid point is based on a local Taylor series expansion. In contrast to the Dirichlet boundary conditions used in Equation 1 as well as in the transport equation for the intermediate velocity of the INS solver, the homogeneous Neumann boundary condition in the Poisson equation requires the use of a 3-D Taylor series expansions of the solution function in the vicinity of irregular grid points. To simplify the analysis in this paper, we will discuss only the 2-D case and note that the same

procedure applies to the 3-D case. The 2-D Taylor series expansion for each grid point, which is part of the finite-difference stencil of the Laplace operator, can be written as

$$\begin{aligned}\phi_{i+1,j+1} = & \phi_{i,j} + \Delta x \phi_x|_{i,j} + \Delta y \phi_y|_{i,j} + \\ & \frac{\Delta x^2}{2!} \phi_{xx}|_{i,j} + \Delta x \Delta y \phi_{xy}|_{i,j} + \frac{\Delta y^2}{2!} \phi_{yy}|_{i,j} + \mathcal{O}(\Delta x^3, \Delta y^3).\end{aligned}\quad (7)$$

Additionally, the boundary condition at the wall-normal intersection point or at the intersection of the immersed boundary with lines of $i = \text{const.}$ and/or $j = \text{const.}$ is considered. Since the wall-normal gradient, $\mathbf{n} \cdot \nabla \phi$, taken at the immersed interface is not aligned with the Cartesian coordinate system, it is useful to introduce a local coordinate system, as presented in Figure 6. Considering the rotation of the local coordinate system with respect to the global coordinate system, the homogeneous Neumann boundary condition can be rewritten as

$$\begin{aligned}\phi_\zeta = & \phi_x \cos(\Theta) + \phi_y \sin(\Theta) + \phi_{xx} \Delta x^* \cos(\Theta) + \\ & \phi_{xy} (\Delta y^* \cos(\Theta) + \Delta x^* \sin(\Theta)) + \phi_{yy} \Delta y^* \sin(\Theta) = 0,\end{aligned}\quad (8)$$

where x^* is the location of the intersection point and $x_{i,j}$ is the location of the irregular grid point such that $\Delta x^* = x^* - x_{i,j}$. In addition to applying the homogeneous Neumann boundary condition, a condition at the boundary can be formulated to utilize the fact that the Neumann boundary condition does not change along the immersed boundary. In mathematical terms, this means that

$$\phi_{\zeta\eta} - \kappa'' \phi_\eta = 0, \quad (9)$$

where κ'' is the curvature of the immersed interface at the intersection point (x^*, y^*) . This yields an additional equation in terms of the horizontal and vertical boundary distances $(\Delta x^*, \Delta y^*)$,

$$\begin{aligned}\phi_{\zeta\eta} - \kappa'' \phi_\eta = & \phi_x \kappa'' \sin(\Theta) - \phi_y \kappa'' \cos(\Theta) + \phi_{xx} (-\sin(\Theta) \cos(\Theta) + \kappa'' \Delta x^* \sin) + \\ & \phi_{xy} (-\sin^2(\Theta) + \cos^2(\Theta) + \Delta y^* \kappa'' \sin(\Theta) - \kappa'' \Delta x^* \cos(\Theta)) + \\ & \phi_{yy} (\sin(\Theta) \cos(\Theta) - \kappa'' \Delta y^* \cos(\Theta)) = 0.\end{aligned}\quad (10)$$

The stencil coefficients of the Laplace operator in the Poisson equation can be derived by balancing the continuous Laplace operator evaluated at $x_{i,j}$ with the discrete Laplace stencil within the order of the truncation error. The Laplace stencil can be written in discrete form as

$$\nabla^2 \phi \Big|_i \approx \sum_{k=1}^n c_k \phi_{i+i_k, j+j_k}, \quad (11)$$

where c_k is the stencil coefficient at the grid point with the indices $i + i_k$ and $j + j_k \in \Omega^+$.

As for the advection-diffusion operator in Equation 1, the Poisson stencil includes more grid points than actually needed to achieve the desired order of accuracy. The occurring over-determined system of equations is solved by considering the Gerschgorin stability conditions for the coefficient matrix, $\underline{\mathbf{M}}$, with the entries m_{ij} given as

$$\sum_{j, j \neq i} |m_{ij}| \leq |m_{ii}|, \quad \text{and} \quad (12)$$

$$m_{ii} \leq 0. \quad (13)$$

When the Gerschgorin condition is satisfied, all eigenvalues of the discretization matrix lie in the left-half side of the complex plane. Additionally, the discrete maximum principle is also satisfied (see Ciarlet [14] for more details). In the present case, the stencil coefficients, c_k , are the solution of a constrained optimization problem:

$$\begin{aligned}f(\mathbf{c}) = & \mathbf{c}^T \cdot \underline{\mathbf{Q}} \cdot \mathbf{c} \longrightarrow \min. \\ \text{with } & \underline{\mathbf{M}} \cdot \mathbf{c} = \mathbf{r}, \quad c_1 \geq 0 \text{ and } c_k \leq 0 \text{ with } k \in \mathbb{N}_{k>1},\end{aligned}\quad (14)$$

where the matrix \mathbf{Q} contains the weights for the different stencil coefficients c_k , and the linear system of equations ensures the formal order of accuracy of the finite-difference discretization. The stencil coefficient c_1 is associated with the grid point at $x_{i,j,k}$. For the solution of the Poisson equation, a multigrid algorithm is employed where the prolongation and restriction operators are adjusted in the vicinity of the immersed boundary similarly to the Laplace-operator discussed above. Introductory texts about multigrid techniques can be found in Brandt [1, 2], Hackbusch [21], Briggs [12], and McCormick [29]. A multigrid algorithm has been developed that uses an Incomplete Line LU (ILLU) decomposition relaxation (see Hemker and Zeeuw [23] and Sonneveld and Zeeuw [38]). The restriction and prolongation operators are derived in a similar way as they were discussed by Zeeuw [45]. In this approach the prolongation, P_k , the restriction, R_k , and the Laplace, L_k , operators on grid point, k , are derived from the fine grid Laplace operator instead of deriving the different operators independently on each grid level. In order to derive the operators on the coarser grids, the following relationships between the prolongation, restriction, and coarse grid Laplace operators are used (see Zeeuw [45]):

$$R_{l-1} = P_l^T \text{ and} \quad (15a)$$

$$L_{l-1} = R_{l-1}L_lP_l, \quad (15b)$$

where $l \in [2, \dots, L]$ and L is the total number of grid levels. The two equations can be used to compute the restriction, R_l , and the coarse-grid Laplace, L_l , operators. A detailed derivation of the prolongation operator, P_l , is provided in Zeeuw [45].

To confirm the order of accuracy of the discrete Laplace-operator with immersed boundary treatment, an analytic test function was assumed in the form of

$$\phi = (x - x_0)^2 + (y - y_0)^2 - D\sqrt{(x - x_0)^2 + (y - y_0)^2}, \quad (16)$$

where ϕ fulfills homogeneous Neumann boundary conditions on the immersed circle centered around (x_0, y_0) . For the error study, a circle with diameter $D = 0.2$ centered around $(x_0, y_0) = (0.5, 0.5)$ was immersed into a computational domain with a length, $L = 1$, and a height, $H = 1$. The results of the error study of the discrete Laplace-operator presented in Figure 7a demonstrate that the discrete Laplace-operator is second-order accurate for the error measured in L_2 -norm and L_∞ -norm.

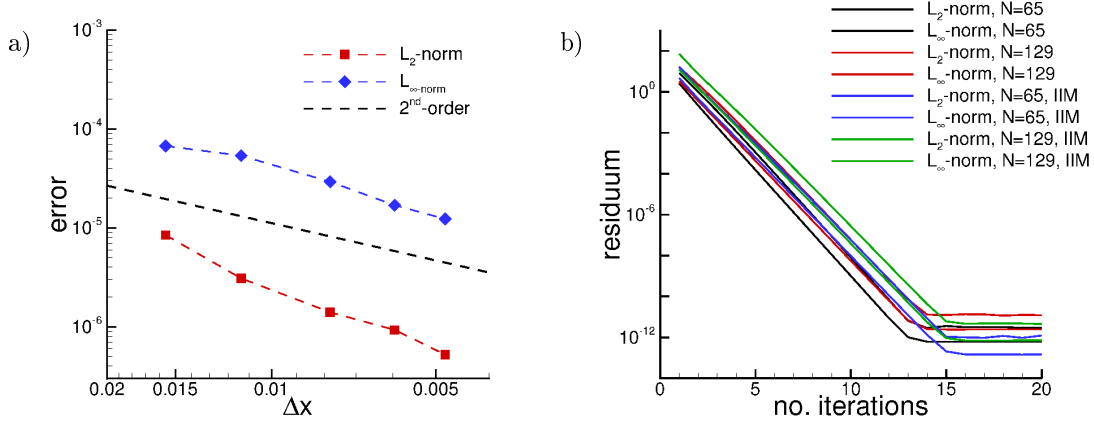


Figure 7: a) Error study of the discrete Laplace operator, and b) L_2 -norm and L_∞ -norm of the residual, $\nabla^2 \cdot \phi - F_{rhs}$, after each V-cycle of the multigrid solver.

In addition, we investigated the convergence behavior of the discretization matrix. Some of the basic properties of the multigrid solver can be identified in Figure 7b. Figure 7b displays the L_2 -norm and L_∞ -norm of the residual, $\nabla^2 \cdot \phi - F_{rhs}$, after each V-cycle of the multigrid solver. Note that for the calculation with an immersed circle, the same setup and solution were used as for the error study of the discrete Laplace-operator displayed in Figure 7a. For the calculations without an immersed boundary, a different analytical solution, $\phi = \sin(2\pi x)\sin(2\pi y)$, was assumed due to the apparent singularity of the solution function, ϕ ,

in Equation 16 at $(x, y) = (x_0, y_0)$. The multigrid convergence rate is unaffected by the difference in the analytical solutions (or right-hand-side forcing terms), because it is a property of the discretization matrix and the applied solution procedure. Four grid levels were assumed for the calculations with $N = 65$ and five grid levels for $N = 129$. The number of grid levels was chosen so that the number of grid points on the coarsest grid level are the same. The convergence rate for $N = 65$ and $N = 129$ are identical, because the coarsest grid determines the convergence rate of the multigrid solver. Further, we noticed that the boundary treatment did not affect the convergence rate of the multigrid solver. Hence, it can be recognized that the desired objective of closely mimicking the spectral behavior of the ideal discretization matrix has been realized by the immersed scheme.

3.2 Higher-Order

Having discussed the basic ideas of the immersed scheme, a higher-order extension of the approach is next introduced. It is evident that higher-order schemes have great advantages with regard to the accuracy of the numerical schemes as well as the computational efficiency of the solver. Higher-order schemes, such as methods developed by Linnick and Fasel [28] and Meitz and Fasel [30], have been shown to achieve a much greater accuracy for a given number of operations than lower-order schemes, which makes higher-order schemes computationally more efficient. However, for immersed boundary methods, the development of higher-order schemes is more complex, because the boundary discretization may become very unstable when increasing the width of the standard finite-difference stencil as shown in Figure 8a. Further, an additional irregular grid point is introduced, as illustrated in Figure 8b. The derivation of the immersed boundary method considering higher-order finite-difference discretization is similar to the previous derivations.

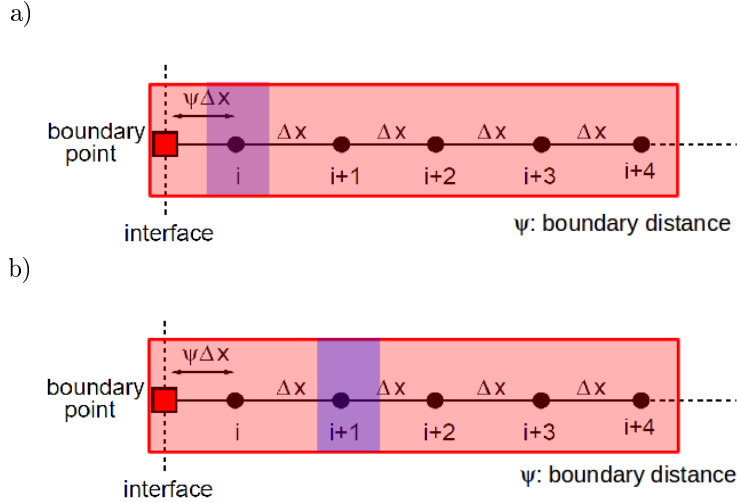


Figure 8: Higher-order finite-difference stencil at irregular grid points (a) x_i and (b) x_{i+1} including boundary point and neighboring grid points in red-shaded region.

We assumed an advection-diffusion-type equation described by Equation 1 with a fourth-order central finite-difference approximation of the first-derivative,

$$\frac{\partial \phi}{\partial x} \Big|_i = \frac{\phi_{i-2} - 8\phi_{i-1} + 8\phi_{i+1} - \phi_{i+2}}{12\Delta x} + \mathcal{O}(\Delta x^4), \quad (17)$$

and a fourth-order accurate discretization of the second-derivative,

$$\frac{\partial^2 \phi}{\partial x^2} \Big|_i = \frac{-\phi_{i-2} + 16\phi_{i-1} - 30\phi_i + 16\phi_{i+1} - \phi_{i+2}}{12\Delta x^2} + \mathcal{O}(\Delta x^4). \quad (18)$$

For a fourth-order accurate scheme based on centered finite-difference stencils, two irregular grid points in

the vicinity of the boundary need to be considered (see Figure 8a and 8b). Since the two grid points are direct neighbors, one may consider formulating a two-dimensional optimization problem, where each free parameter is associated with one irregular grid point. For the results shown in this section, the two free parameters were determined by sequentially solving two one-dimensional optimization problems instead of solving a two-dimensional optimization problem. First, the finite-difference stencil coefficients for the grid point closest to the boundary, x_i , is determined and then coefficients for the neighboring grid point, x_{i+1} . We utilized six grid points of the finite-difference stencils at both irregular grid points, x_i and x_{i+1} . In principal, only five grid points are needed to formally achieve a third-order accurate finite-difference approximation of the continuous equation at the boundary stencils. Again, the additional stencil coefficient is used to optimize the finite-difference scheme by minimizing the L_2 -norm of the perturbation matrix, $\underline{\mathbf{E}}$. It should be noted that in the case of no diffusion ($\beta = 0$), the finite-difference scheme is fourth-order accurate for the advection terms.

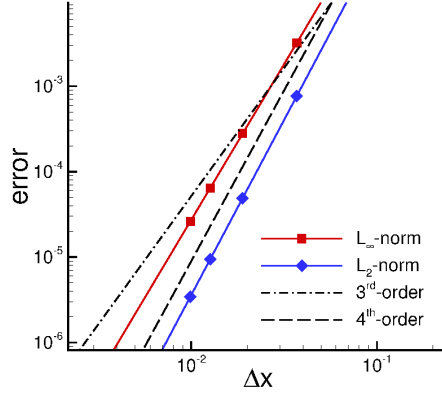


Figure 9: Error study of the discrete spatial operator of Equation 1 measured in L_2 -norm (squares) and L_∞ -norm (diamonds).

Figure 9 illustrates that a high-order accurate finite-difference scheme can be achieved with this approach. The error study of the discrete spatial operator of $-c_x \phi_x + \mu \phi_{xx}$ demonstrates that fourth-order accuracy can be achieved in the L_2 -norm and the scheme is at least third-order accurate in the L_∞ -norm.

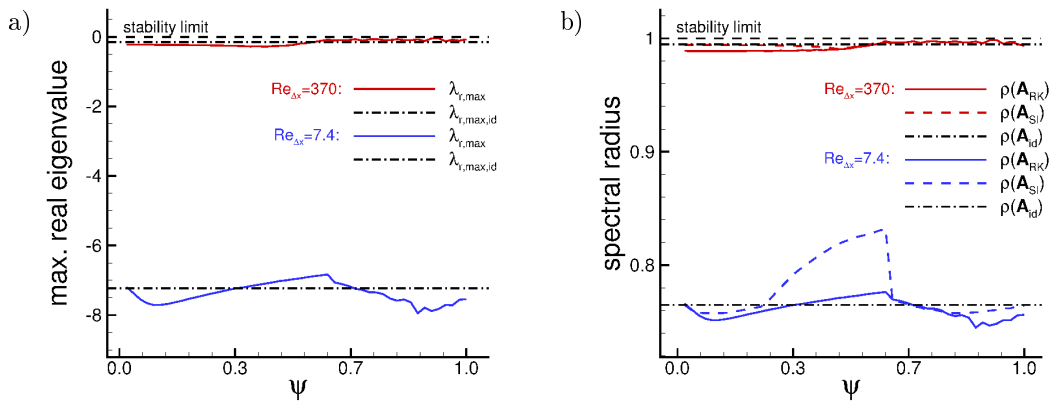


Figure 10: *a)* Maximum real eigenvalue, $\lambda_{r,max}$, of the spatial discretization matrix, $\tilde{\mathbf{A}}$, and *b)* spectral radius of combined spatial and temporal discretization matrix, $\underline{\mathbf{A}}$, for a boundary distance of $0 \leq \psi \leq 1$. $Re_{\Delta x}$ is the cell Reynolds number defined as $Re_{\Delta x} = \Delta x c_x / \beta$.

Figure 10 presents the results of a stability analysis of the high-order immersed boundary method for a boundary distance of $0 \leq \psi \leq 1$ and different cell Reynolds numbers. The advection speed was taken to be $c_x = 1$, which from a numerical stability point-of-view, is the most difficult case to stabilize since the flow moves away from the surface. The matrix stability analysis results confirm that a stable explicit and implicit time-integration can be achieved with the high-order extension of the immersed boundary method. For the explicit time-integration we employed the standard fourth-order accurate Runge-Kutta scheme (RK4) and the semi-implicit second-order accurate time scheme (SI) is based on the trapezoidal rule.

$$\underline{\mathbf{A}}_{RK} = \mathbf{I} + \frac{\Delta t}{1!} \tilde{\mathbf{A}} + \frac{\Delta t^2}{2!} \tilde{\mathbf{A}}^2 + \frac{\Delta t^3}{3!} \tilde{\mathbf{A}}^3 + \frac{\Delta t^4}{4!} \tilde{\mathbf{A}}^4 \quad \text{and} \quad \underline{\mathbf{A}}_{SI} = \left(\mathbf{I} - \frac{\Delta t}{2} \tilde{\mathbf{A}} \right)^{-1} \left(\mathbf{I} + \frac{\Delta t}{2} \tilde{\mathbf{A}} \right) \quad (19)$$

As before, we refer to the “ideal” discretization matrix with the subscript “id”.

3.3 Incompressible Navier-Stokes Solver

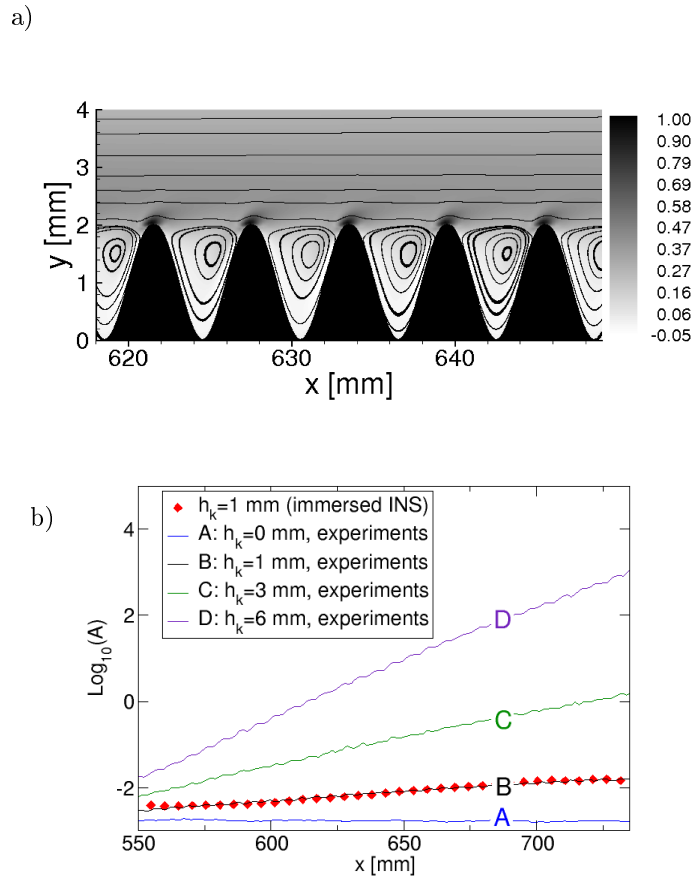


Figure 11: a) Streamlines and contours of constant vorticity, ω_z , for sinusoidal roughness elements with a spacing of $\lambda_R = 6 \text{ mm}$ and height of $h_k = 2.0 \text{ mm}$ and b) comparison of amplitude curves extracted from experimental study by Gaster [19] for a roughness height of $h_k = 1 \text{ mm}$.

At this point, all the essential extensions of the current immersed boundary method are available so the combination can be utilized for solving the incompressible Navier-Stokes equations. After discussing the theoretical concept of the immersed boundary method, some simulation results using the current approach are presented. The immersed, incompressible Navier-Stokes solver has been applied to a variety of applications, e.g. flow past distributed roughness (Brehm *et al.* [10]), pulsatile, stenotic flows (Brehm *et al.* [8]), biglobal

stability analysis and direct numerical simulations of the flow past a NACA0015 airfoil (Brehm *et al.* [6]). Some of these results are shortly discussed below.

In Brehm *et al.* [10], the method presented herein has been used in an incompressible Navier-Stokes solver to investigate the stability behavior of a Blasius boundary layer flow over a wavy wall. This is a very challenging test-case for the immersed boundary method, because for stability calculations, the accuracy in the vicinity of wall is crucial for the precise prediction of the stability characteristics of the mean flow. Different parameters such as the shape, height, and the spacing of the wall waviness were investigated in this study. Figure 11a shows streamlines and contours of spanwise vorticity of the mean flow for sinusoidally shaped elements. The mean flow is characterized by pockets of recirculation between two sinusoidal elements. The actual instability wave enters these pockets and experiences local acceleration and deceleration. The stability investigations showed that the distributed sinusoidal elements, which were characterized by their spacing, λ_R , and their height, h_k , can have a strong impact on the stability of the mean flow. Figure 11b displays a comparison between amplitude curves extracted from an experimental study by Gaster [19] and our numerical investigations for a roughness spacing of $\lambda_R = 6 \text{ mm}$ and height of $h_k = 1 \text{ mm}$. The results obtained from the stability analysis investigation of the mean flow past a wavy wall are in agreement with the experimental observations by Gaster [19].

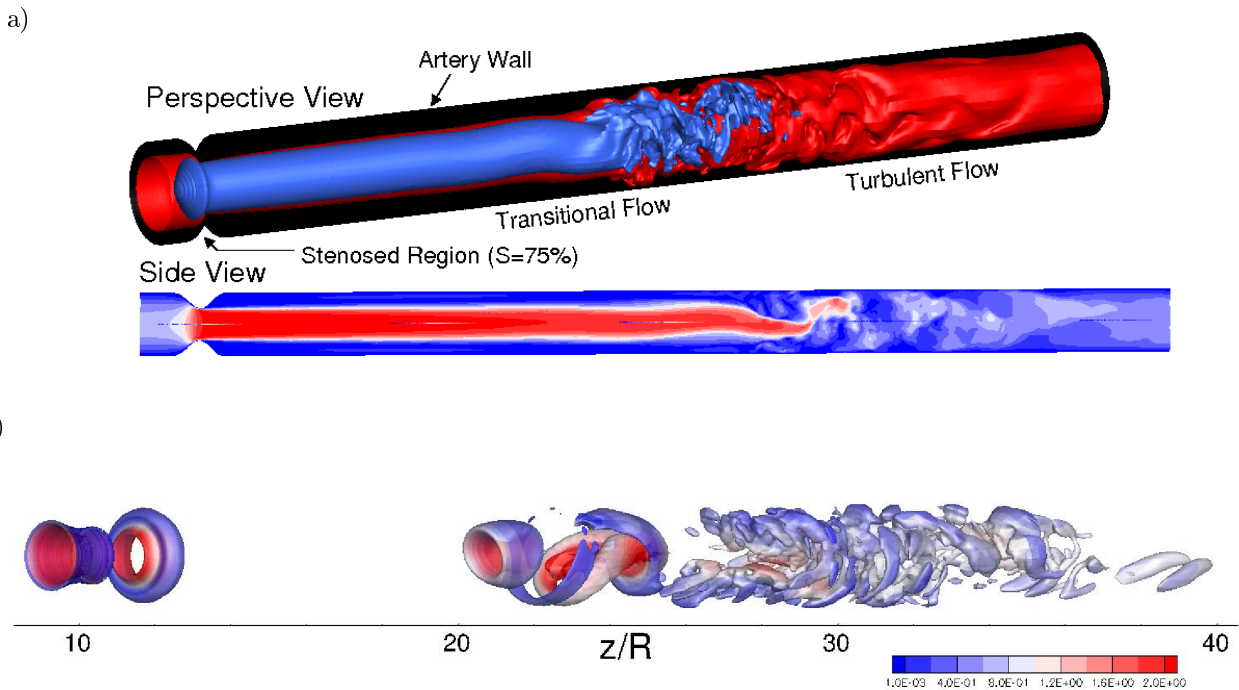


Figure 12: *a)* Instantaneous iso surfaces of absolute velocity illustrating laminar-turbulent transition of stenotic jet for $Re = 750$ and $S = 75\%$. *b)* Instantaneous contour surfaces of $Q = 0.12$ (Q-criterion) and contours of wall pressure in the background for $U_{red} = 2.5$, $Re = 425$, $S = 75\%$, $\lambda/R = 4$ and $\bar{u}_{peak}/\bar{u}_m = 1.75$.

In another application, the immersed boundary method was used together with the incompressible Navier-Stokes solver to study the flow through constricted tubes, which serve as a model for stenosed arteries (see Brehm *et al.* [8]). The immersed boundary approach is very useful for the simulation of biofluid dynamics problems because the Reynolds numbers are very small and fluid-structure-interaction problems can be handled very well. The artery tree in the human body provides a great variety of different shapes with complicated 3-D bends and continuously changing artery diameters. In Brehm *et al.* [8], the transition process of steady and pulsatile flows was investigated by employing Floquet-type analysis and DNS. Figure 12a visualizes the velocity field for a flow through a contraction (or stenosis) for a degree of stenosis of $S = 75\%$ and a Reynolds number of $Re = 750$. For this calculation we used a steady inflow profile. Figure

12b shows simulation results considering an unsteady velocity inflow profile for a Reynolds number, $Re = 425$, a degree of stenosis, $S = 75\%$, a stenosis length, $\lambda/R = 4$, a peak to mean velocity ratio, $\bar{u}_{peak}/\bar{u}_m = 1.75$, and a reduced velocity, $U_{red} = 2.5$.

3.4 Compressible Navier-Stokes Equations

Several additional features need to be accounted for when applying the immersed boundary treatment to the compressible Navier-Stokes equations instead of the linear 1-D advection-diffusion equation used in section 2: (1) the compressible Navier-Stokes equations are strongly non-linear; (2) we need to work with a coupled system of equations; and (3) the flux-splitting scheme needs to be included in the analysis. The interior discretization of the 1-D Euler equation is identical to the approach presented in Laible and Fasel [26]. A standard fourth-order accurate Runge-Kutta scheme is used for time-integration. The forward-flux, \mathbf{F}_x^+ , and the backward-flux, \mathbf{F}_x^- , are discretized with ninth-order accurate grid-centered upwind differences as proposed by Zhong [46]. As in Laible and Fasel [26], a parameter α is used to determine the degree of upwinding for the grid-centered upwind differences

$$\left. \frac{\partial \phi}{\partial x} \right|_i = \sum_{k=i-N}^{i+N} c_k \phi_k - \alpha \overline{\Delta x} \left. \frac{\partial^{2N-1} \phi}{\partial x^{2N-1}} \right|_i, \quad (20)$$

where c_k is the stencil coefficient, $\overline{\Delta x}$ is the averaged grid spacing over the spatial extent of the stencil and N determines the number of grid points in the stencil. Note that a central difference stencil can be achieved by choosing $\alpha=0$. In accordance to the chosen discretization in Laible and Fasel [26], the ninth-order upwind stencils are calculated with $N = 5$ and $\alpha = -1500$. For the present results, van Leer's flux splitting scheme [41] was utilized. It should be noted that it is expected that applying flux splitting at irregular grid points may help to stabilize the finite-difference stencils, because numerical dissipation is introduced from the splitting direction pointing away from the wall. The Euler-equations are integrated in time with a fourth-order accurate Runge-Kutta time-integration scheme. For further details about the interior scheme of the compressible Navier-Stokes solver employed, see Fasel and Laible [26]. Details regarding the diffusion terms are provided in Brehm *et al.* [9], where the full implementation of the immersed scheme into the compressible Navier-Stokes equations is discussed and analyzed in detail.

Next, the basic ideas of the IIM implementation are briefly discussed for the 1-D Euler equations in a conservative variable formulation,

$$\begin{pmatrix} \rho \\ \rho u \\ E_t \end{pmatrix}_t = \begin{pmatrix} \rho u \\ \rho u^2 + p \\ u(E_t + p) \end{pmatrix}_x, \quad (21)$$

where the total energy can be expressed as $E_t = \rho(T/((\gamma - 1)\gamma M^2) + u^2/2)$. The fluid is assumed to be an ideal gas, which can be modeled by the equation of state $p = 1/(\gamma M^2)\rho T$. In this analysis, the viscous effects are not included, since it is assumed that adding diffusion appears to stabilize rather than destabilize the numerical scheme.

The 1-D Euler equations, after applying van Leer's flux splitting approach, can be written as

$$\mathbf{u}_t + \mathbf{F}_x = \mathbf{u}_t + \mathbf{F}_x^- + \mathbf{F}_x^+ = 0, \quad (22)$$

where the solution vector has the form $\mathbf{u} = (u_1, u_2, u_3)^T = (\rho, \rho u, E_t)^T$. In order to apply linear stability analysis theory, the 1-D Euler system in Equation 22 is linearized by introducing the Jacobian, $\partial \mathbf{F} / \partial \mathbf{u}$, and holding it constant through a single time-step.

$$\mathbf{u}_t = -\frac{\partial \mathbf{F}}{\partial \mathbf{u}} \cdot \frac{\partial \mathbf{u}}{\partial x} = -\frac{\partial \mathbf{F}^-}{\partial \mathbf{u}} \cdot \frac{\partial \mathbf{u}}{\partial x^-} - \frac{\partial \mathbf{F}^+}{\partial \mathbf{u}} \cdot \frac{\partial \mathbf{u}}{\partial x^+}. \quad (23)$$

Equation 24 contains the derivatives of the forward/backward-flux vectors, \mathbf{F}^\pm , with respect to the solution

vector \mathbf{u} .

$$\begin{aligned}\mathbf{u}_t &= -\frac{\partial \mathbf{F}^+}{\partial \mathbf{u}} \cdot \frac{\partial \mathbf{u}}{\partial x^+} - \frac{\partial \mathbf{F}^-}{\partial \mathbf{u}} \cdot \frac{\partial \mathbf{u}}{\partial x^-} \\ &= -\frac{\partial \mathbf{F}^+}{\partial \mathbf{u}} \cdot (\mathbf{D}_x^+ \cdot \mathbf{u}) - \frac{\partial \mathbf{F}^-}{\partial \mathbf{u}} \cdot (\mathbf{D}_x^- \cdot \mathbf{u}).\end{aligned}\tag{24}$$

In the current finite-difference scheme, the gradient of the forward-flux is discretized with a forward difference operator, \mathbf{D}_x^+ , and the gradient of the backward flux is discretized with a backward difference operator, \mathbf{D}_x^- . The details regarding the structure of the forward and backward difference operators, \mathbf{D}_x^\pm , are provided in Brehm *et al.* [9]. The derivation of the over-determined system of equations governing the finite-difference stencil coefficients is similar to the approach outlined above for the 1-D advection-diffusion equation. The coupling of the three (four for 2-D and five for 3-D) conservative variables simply increases the dimension of the perturbation matrix \mathbf{E} by a factor of three (four for 2-D and five for 3-D).

For numerical analysis of the boundary stencils, the equations are considered in terms of the numerical error vector, $\boldsymbol{\varepsilon}$,

$$\boldsymbol{\varepsilon}_t = -\frac{\partial \mathbf{F}^+}{\partial \mathbf{u}} \cdot (\mathbf{D}_x^+ \cdot \boldsymbol{\varepsilon}) - \frac{\partial \mathbf{F}^-}{\partial \mathbf{u}} \cdot (\mathbf{D}_x^- \cdot \boldsymbol{\varepsilon}).\tag{25}$$

Note that for the numerical analysis of the scheme, it is assumed that the components of the Jacobian are “frozen” and independent of the error vector, $\boldsymbol{\varepsilon}$. Moreover, it can be readily recognized that homogeneous boundary conditions can be applied to the error vector without a loss of generality. For the chosen ninth-order accurate interior, spatial discretization with a stencil half-width of five grid points, it is necessary to adjust the five grid stencils, which are in the direct vicinity of the immersed boundary. Due to the flux splitting approach, only one of the spatial (forward or backward) discretization matrices (\mathbf{D}_x^+ or \mathbf{D}_x^-) requires a special boundary treatment so that a local numerical instability can be avoided.

The Jacobian of the total flux vector, $\mathbf{J}_F = \partial \mathbf{F} / \partial \mathbf{u}$, and the Jacobian of the forward flux vector, $\mathbf{J}_{F^+} = \partial \mathbf{F}^+ / \partial \mathbf{u}$, are displayed in Brehm *et al.* [9]. The strategy for determining the stencil coefficients at irregular grid points is identical to the approach for the advection-diffusion equation presented above.

A comparison with other possible immersed boundary approaches is shown in Figure 13. In this analysis, we considered four different strategies which could be used to determine irregular grid stencils. The first scheme includes grid points at $x_{\partial\Omega}$, x_i , x_{i+1} and x_{i+2} , and computes their corresponding coefficients by applying a least-squares polynomial fit. Four grid points are used to overcome the singularity at $\psi = 0$, which is present for the second approach. The second approach, which uses an exact polynomial fit considering the three grid points $x_{\partial\Omega}$, x_i , and x_{i+1} , was only chosen for comparison purposes. Due to the apparent singularity at $\psi = 0$, it was not expected that this approach would perform well for small ψ . In the literature (see for example Linnick and Fasel [28]), it has been suggested that one can overcome this problem, namely the first-order singularity ($1/\psi$) at $\psi = 0$, by omitting grid point x_i in the finite-difference stencil, and instead of x_i , use grid point x_{i+2} in the finite-difference stencil. The immersed boundary approach proposed in this work is the third method considered for comparison and is denoted by $x_k \in [x_{\partial\Omega}, x_{i+1}, x_{i+2}]$. In a fourth scheme, only regular finite-difference stencils are considered, and it is, therefore, referred to as the “ideal” scheme. It is referred to as “ideal”, because it contains the spectral properties, which we attempt to closely mimic with an immersed boundary discretization.

In Figure 13, the spectral radius of the full discretization matrix, \mathbf{A} , of each immersed approach is plotted for different boundary distances, ψ , to compare the spectral radii of these methods. In order to get an idea about the behavior of the undisturbed numerical scheme, the spectral radius of the ideal discretization matrix is shown as a solid black line. Note, that since the computational domains for the ideal discretization matrix and the immersed schemes are slightly different (on the order of $\mathcal{O}(L/(N-1))$), a small deviation in the eigenvalues is expected. However, this difference is negligible, and the spectral radius of the ideal scheme provides a quality measure for the immersed schemes.

For the stability results presented herein, the final discretization matrices (including the entire computational domain) are considered, and a standard fourth-order accurate Runge-Kutta time-integrator was utilized with $CFL \approx 0.69$. The CFL -number is based on the smallest grid spacing and the maximum

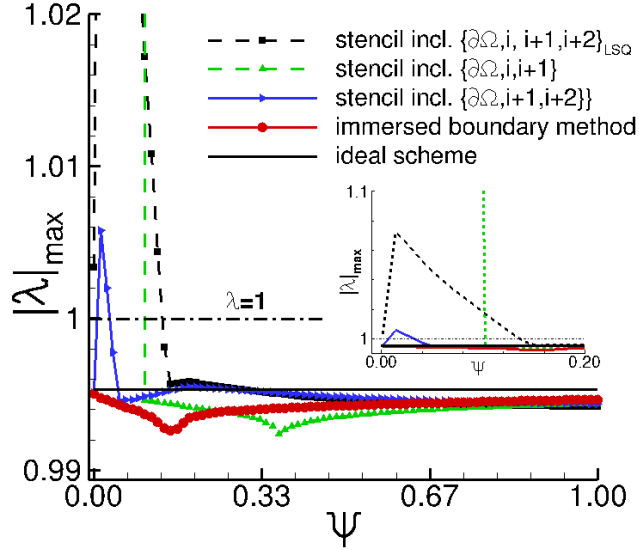


Figure 13: Comparison of four strategies to determine irregular grid stencils. The spectral radius, $\rho(\underline{\mathbf{A}}) = |\lambda|_{max}$, is plotted for different boundary distances, ψ .

velocity plus the speed of sound:

$$CFL = ||u|_{max} + c| \frac{\Delta t}{\Delta x} \quad \text{with } |u|_{max} = 1 \quad \text{and } c = \frac{1}{M} = \frac{1}{6} \quad \text{leads to } CFL = \frac{7\Delta t}{6\Delta x}. \quad (26)$$

The first observation is that none of the three alternative immersed schemes are stable over the full range of $0 < \psi \leq 1$. From the three alternative schemes, the third scheme has the smallest unstable region between $\psi \simeq 0.0067$ and $\psi \simeq 0.0323$. The inset (smaller plot) in Figure 13 is included to provide a close-up of the region, $0 < \psi \leq 0.2$, to indicate the magnitude of the spectral radii in this region. As discussed above, the second scheme is unbounded for small ψ due to the singularity at $\psi = 0$. The least-squares polynomial fit approach shows bounded spectral radii for ψ approaching zero, but it contains the largest unstable region, between $\psi \simeq 0.0$ and $\psi \simeq 0.136$, of all three alternative immersed schemes. The spectral radii for the proposed immersed boundary approach are all smaller than the spectral radius of the ideal scheme. The most likely explanation for this observation is that the immersed boundary treatment leads to a small increase of numerical damping, which reduces the magnitude of the spectral radii. The largest deviation of the spectral radius from the “ideal” scheme can be observed in the region where the three alternative immersed schemes become unstable. The minimum value of the spectral radius is 0.9926, and it presents the largest deviation (approximately 0.2%) from the spectral radius, $|\lambda|_{max} = 0.9946$, reached at $\psi = 1$. Hence, the change of the spectral radius with respect to the boundary distance is very small for the presented immersed approach. Moreover, it can be concluded that for the present test-case, the approach applied to the 1-D Euler equations satisfies the necessary condition for stability.

The presented immersed boundary scheme for the compressible Navier-Stokes equations was successfully employed for Temporal Direct Numerical Simulations (*TDNS*) of instability waves in a Mach 6 boundary layer over a porous wall. Previous research studies have shown that porous wall can have a significant stabilization effect on the temporal/spatial growth of disturbances in a boundary layer flow (see for example Malmuth *et al.* [33], Federov *et al.* [17, 16], Bres *et al.* [11], Sandham and Lüdeke [37], and Hader and Fasel [22]). The effect of various geometric parameters, such as the depth of the porous layer, d , the porosity, ϕ , and the number of pores per wave length, n_p , on the growth of disturbances in the boundary layer has been investigated. Figure 14 shows a comparison of the temporal growth rate, ω_i , for different porous layer depth, d , between Linear Stability Theory (*LST*) results by Federov *et al.* [17], DNS results by Wartemann *et al.* [42], DNS results employing direct forcing by Hader and Fasel [22] and the presented immersed boundary

method.

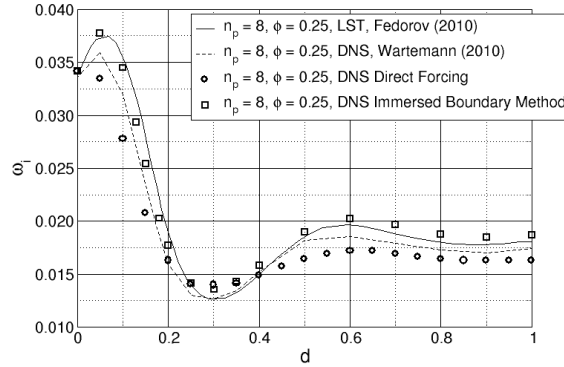


Figure 14: Comparison of temporal growth rate, ω_i , for varying porous layer depth, d , between LST results by Federov *et al.* [17], DNS results by Wartemann *et al.* [42], DNS results employing direct forcing by Hader and Fasel [22] and the presented immersed boundary method.

The results employing the presented immersed boundary method are in excellent agreement with the theoretical results by Federov *et al.* [15] as shown in Figure 14. Even the region of destabilization between $d = 0$ and $d \approx 0.1$ is predicted correctly. It must be noted that the immersed boundary method, which was previously used for porous wall calculations, based on a direct forcing approach presented in Hader and Fasel [22] was not able to resolve this region. It must be emphasized that the near wall accuracy, in particular the phase relation between wave velocity components close to the wall, is critical to obtain accurate results for these stability investigations.

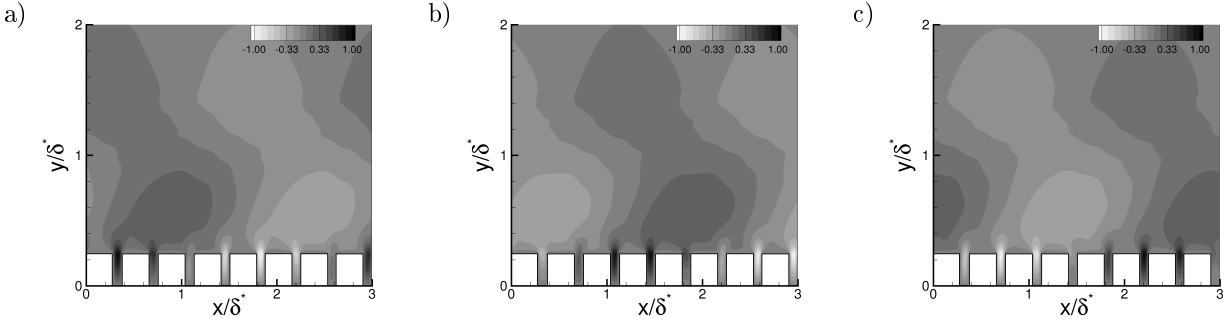


Figure 15: Snapshots of v' -velocity for a) $t=0$, b) $t=T/3$, and c) $t=2T/3$ illustrating the interaction of second mode instability wave with porous wall ($n_p = 8$, $d = 0.25$, and $\phi = 25$).

Figure 15 shows snapshots of v' -velocity for three instances in time over one forcing period, T . A strong impact of the porous wall on the disturbance flow field can be noted, where large amplitudes of v' -velocity are present in between the pores. The large amplitudes of v' -velocity in the vertical gaps are related to underlying physical mechanism, which drives the disturbance flow field in and out of the cavities. This unsteady vertical motion in and out of the cavities may be responsible for reducing the amplitude growth of the instability wave. The immersed boundary method permits investigations of the flow characteristics within these cavities in much more detail when compared to the IBT used in Hader and Fasel [22]. The more accurate, immersed method leads to significant reduction in numerical noise in the vicinity of the porous wall, and therefore, leads to more accurate and reliable simulation results.

3.5 Maxwell's Equations

In this section, the immersed boundary method is extended to a partial-differential equation with coefficients containing spatial discontinuities. The Maxwell's equations are taken as an example to briefly discuss the necessary steps to extend the immersed method to these types of equations. Since the issue of dealing with coupled systems of equations has already been discussed in the compressible Navier-Stokes section we will only introduce the new aspect of spatially discontinuous coefficients for the current immersed method.

A 1-D model of the linear Maxwell's equations in an isotropic, homogeneous, non-dispersive media can be written as

$$\epsilon \frac{\partial E}{\partial t} = \frac{\partial H}{\partial x} \quad \text{and} \quad (27a)$$

$$\mu \frac{\partial H}{\partial t} = \frac{\partial E}{\partial x}, \quad (27b)$$

where E and H are the electric and magnetic field intensities, respectively. In this equation, it is assumed that the permittivity of the material, ϵ , and the permeability of the material, μ , can be a function of space and that at the interface location, $x = x_\alpha$, both quantities can be discontinuous.

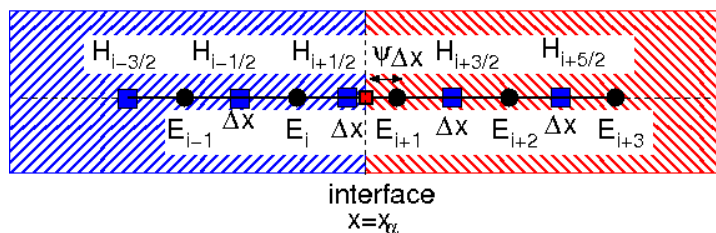


Figure 16: Computational setup for solving the Maxwell's equations.

Figure 16 shows the computational layout considered for solving the 1-D Maxwell's equations. The Maxwell's equations are solved on a staggered mesh by employing the Yee scheme [44]. For the configuration displayed in Figure 16, the two grid stencils for $H_{x,i+1/2}$ and $E_{x,i+1}$ cross the interface at $x = x_\alpha$ and must, therefore, be corrected. Since we assumed a spatial discontinuity of the material properties at $x = x_\alpha$, which leads to a discontinuity in the solution function, the jump corrected Taylor series expansion (see Wiegmann and Bube [43]) needs to be considered. The Taylor series of functions with jump singularities,

$$f(x_{i+1}) = f(x_i) + f'(x_i) \Delta x + f''(x_i) \frac{\Delta x}{2!} + \dots + J_{x=\alpha}, \quad (28)$$

includes jump correction terms, $J_{x=\alpha}$, at the location of the singularity, $x = x_\alpha$, which can be written as

$$J_{x=\alpha} = [f]_{x=\alpha} + [f']_{x=\alpha} \Delta x^+ + [f'']_{x=\alpha} \frac{\Delta x^+}{2!} + \dots, \quad (29)$$

with the grid spacing, $\Delta x = x_{i+1} - x_i$, and the distance to interface on the left $\Delta x^+ = x_{i+1} - x_\alpha$. The term $[f]_{x=\alpha}$ represents the jump in the value of f at $x = \alpha$, which is defined by

$$[f]_{x=\alpha} = \lim_{x \rightarrow \alpha^+} f(x) - \lim_{x \rightarrow \alpha^-} f(x), \quad (30)$$

where $[f']_{x=\alpha}$ represents the jump in the value of the first derivative of the function, and so forth. The jump corrections used in the Taylor series of functions with jump singularities are derived from the continuous Maxwell's equations considering that $[E] = 0$ and $[H] = 0$ at the interface. In addition, it is assumed that both the electric and magnetic field intensities at $x = x_\alpha$ are continuous in time. The procedure for determining the coefficients of finite-difference stencils which cross the material discontinuity at x_α is the same as for the other extensions presented above. For more details about this method see Brehm *et al.* [5].

Figure 17 presents the stability analysis results for a computational domain with a length of $L_x = 1$ and $N = 31$ grid points, assuming $1 \geq \epsilon^+/\epsilon^- \geq 100$, $\mu = 1$, and $0 \geq \psi \geq 0.5$. The difference between the spectral radius of the combined temporal and spatial discretization matrix of the immersed scheme and the

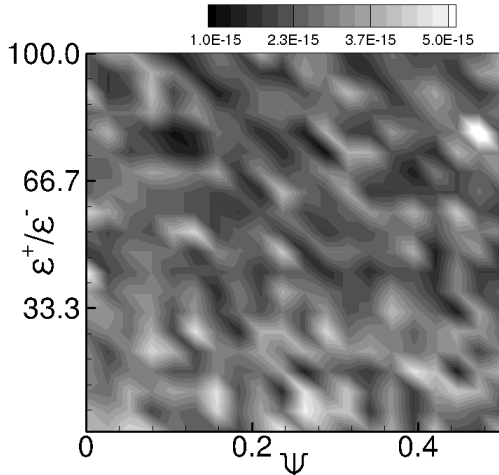


Figure 17: Difference between the spectral radius of the combined temporal and spatial discretization matrix of the immersed scheme and the “ideal” spectral radius, ($\rho_{id} = 1$).

“ideal” spectral radius ($\rho_{id} = 1$) is within round-off accuracy for all investigated combinations of ϵ^+/ϵ^- and ψ . It should be noted that Equations 27a-27b describe the propagation of electromagnetic waves in an ideal (loss-less) medium without attenuation—which means that all eigenvalues of the spectrum are supposed to be on the unit circle. The Yee-scheme fulfills this property making it difficult to design a robust immersed method for this scheme, because a small perturbation may push an eigenvalue outside the unit circle leading to numerical instability. It follows from the foregoing that the stability analysis results indicate that a stable time-integration can be achieved for solving the Maxwell’s equations including discontinuous material properties with the present immersed interface approach.

3.6 Moving Boundary

In the context of solving the advection-diffusion equation incorporating moving boundaries, the method presented herein can be viewed as an Eulerian-Lagrangian formulation. This means that the governing equations are solved in an Eulerian fashion on a stationary grid, and the moving boundaries are tracked in a Lagrangian manner. We believe that the treatment of the governing equation in Eulerian form on stationary, non-deforming grids greatly simplifies the computation of moving boundary problems. It may be recognized that Eulerian-Lagrangian methods considering an immersed boundary method provide more than just an alternative approach to conventional Lagrangian-type methods. In Lagrangian-type approaches, one has to deal with moving/deforming grids and discretized equations, which produce additional time derivatives of grid-related quantities, such as the changing cell volume. Further, for Lagrangian-type methods, large boundary deformations or movements lead to major complications in the local adjustment of the grid in the vicinity of the boundary, such as the occurrence of negative volumes in finite volume formulations.

Figure 18 shows that as the immersed boundary moves across the fixed Cartesian grid, so called “freshly-cleared” cells¹ may appear. For fluid-solid interfaces, these cells are cells in the fluid, which were inside the solid domain at the previous time-step. In effect, the spatial discontinuity will lead to a temporal discontinuity. Thus, a straightforward temporal discretization of the governing equations for these cells is not possible, because these cells do not have a valid time history.

The current numerical scheme will be introduced for the 1-D nonlinear viscous Burgers’ equation,

$$\phi_t = -\phi\phi_x + \mu\phi_{xx}, \quad \text{with} \quad \phi(a, t) = \phi_L, \quad \phi(b, t) = \phi_R \quad \text{and} \quad \phi(x, 0) = \phi_0(x). \quad (31)$$

¹The terminology “freshly-cleared” cells was initially introduced in the context of solving the Navier-Stokes equations within a framework of finite volume solvers. The problem of “freshly-cleared” cells is clearly identical in a finite-difference formulation. However, in the finite-difference context one may refer to these cells as “freshly cleared” grid points.

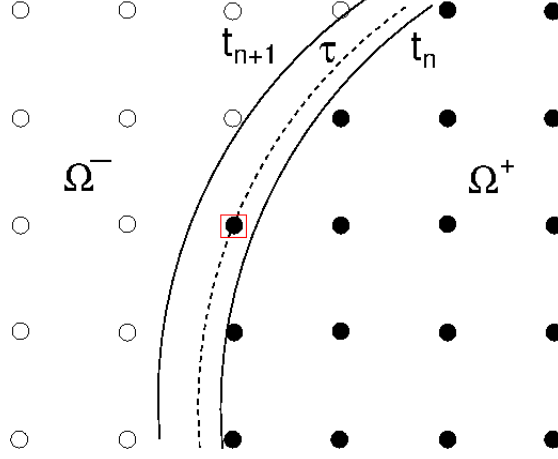


Figure 18: Solid-fluid (Ω^-/Ω^+) interface crosses freshly-cleared grid point (\square) at $t = \tau$. Points inside the fluid domain are marked with solid circles and points in the solid domain are marked with open circles.

The Burgers' equation may serve as a model for the momentum equations describing the fluid motion. Therefore, the scalar quantity, $\phi(x, t)$, in Equation 31 can be interpreted as a 1-D velocity field. Only considering the temporal discretization, the continuous viscous Burgers' equations can be written in semi-discrete form:

$$\frac{\phi_i^{n+1} - \phi_i^n}{\Delta t} = \frac{1}{2} (-\phi_i^n \phi_{x,i}^{n+1} + \mu \phi_{xx,i}^n) + \frac{1}{2} (-\phi_i^{n+1} \phi_{x,i}^n + \mu \phi_{xx,i}^{n+1}), \quad (32)$$

which is an $\mathcal{O}(\Delta t^2)$ numerical approximation of the continuous equation. Note that the convection term at $t_{n+1/2}$ was approximated in a different way than Li and Ito [27] employed, i.e. $(\phi \phi_x)_i^{n+1/2} = \frac{1}{2}(\phi_i^n \phi_{x,i}^n + \phi_i^{n+1} \phi_{x,i}^{n+1}) + \mathcal{O}(\Delta t^2)$. The present approach avoids an additional iteration procedure that does not appear to affect the accuracy. On first glance, the accuracy can be studied by considering the truncation error of these approximations:

$$\begin{aligned} \frac{1}{2} (\phi_i^n \phi_{x,i}^n + \phi_i^{n+1} \phi_{x,i}^{n+1}) &\approx \phi_i^{n+1/2} \phi_{x,i}^{n+1/2} + \\ &\Delta t^2 \left(\frac{1}{2} \phi_{tt,i}^{n+1/2} \phi_{x,i}^{n+1/2} + \phi_{t,i}^{n+1/2} \phi_{xt,i}^{n+1/2} + \frac{1}{2} \phi_i^{n+1/2} \phi_{xtt,i}^{n+1/2} \right) + \mathcal{O}(\geq \Delta t^3) \end{aligned} \quad (33a)$$

and

$$\begin{aligned} \frac{1}{2} (\phi_i^n \phi_{x,i}^{n+1} + \phi_i^{n+1} \phi_{x,i}^n) &\approx \phi_i^{n+1/2} \phi_{x,i}^{n+1/2} + \\ &\Delta t^2 \left(\frac{1}{2} \phi_{tt,i}^{n+1/2} \phi_{x,i}^{n+1/2} - \phi_{t,i}^{n+1/2} \phi_{xt,i}^{n+1/2} + \frac{1}{2} \phi_i^{n+1/2} \phi_{xtt,i}^{n+1/2} \right) + \mathcal{O}(\geq \Delta t^3). \end{aligned} \quad (33b)$$

Equation 32 can be applied to regular and irregular non-“freshly-cleared” grid points. For “freshly-cleared” grid points, the semi-discrete Equation 32 needs to be revised. Two possible strategies will be presented, which take advantage of the fact that the boundary position, velocity, and acceleration are known at all time-steps. First, instead of approximating the right-hand-side of Equation 31 at time-level $n + 1/2$, we considered the right-hand-side at time-levels n and $n + 1$, and therefore the right-hand-side is approximated at time, $(t_{n+1} + \tau)/2$. Hence, the revised version of Equation 32 can be written as

$$\frac{\phi_i^{n+1} - \phi_i^{n\tau}}{t_{n+1} - \tau} = \frac{1}{2} (-\phi_i^{n\tau} \phi_{x,i}^{n+1} + \mu \phi_{xx,i}^{n\tau}) + \frac{1}{2} (-\phi_i^{n+1} \phi_{x,i}^{n\tau} + \mu \phi_{xx,i}^{n+1}), \quad (34)$$

where τ is the time when the boundary crosses grid point x_i . This approach treats the temporal singularity at the “freshly-cleared” grid point in a different fashion than in the approach discussed by Li and Ito [27].

In the current approach, additional kinematic considerations are used to determine the velocities at “freshly-cleared” cells. The key idea is that since the velocity of the boundary is equal to the fluid velocity at the fluid-solid interface, it follows that this information can be used to calculate the fluid velocity at “freshly-cleared” grid points. The velocity, $\phi_i^{n_\tau}$, can be computed by considering Taylor series expansions of the velocity at the Lagrangian marker point on the boundary with respect to the intersection time, τ , and the location of the “freshly-cleared” grid point, x_i ,

$$\begin{aligned} \phi(x = x_b) = \dot{x}_b = & \phi_i^{n_\tau} + \Delta t \phi_{t,i}^{n_\tau} + \Delta x \phi_{x,i}^{n_\tau} + \frac{\Delta t^2}{2!} \phi_{tt,i}^{n_\tau} + \\ & \Delta t \Delta x \phi_{xt,i}^{n_\tau} + \frac{\Delta x^2}{2!} \phi_{xx,i}^{n_\tau} + \mathcal{O}(\Delta x^3, \Delta t^3), \end{aligned} \quad (35)$$

where x_b denotes the location of the moving boundary. Since, the boundary motion is tracked by Lagrangian marker points, it is necessary to consider the substantial (or material) derivative. This expression is very useful, because it allows the time derivative in Eulerian variables to be computed similar to following a material particle. Assuming that $\partial()/\partial \hat{t}$ denotes the temporal derivative from a Lagrangian viewpoint, the Eulerian substantial derivative can be written as

$$\frac{\partial()}{\partial \hat{t}} \equiv \frac{\partial()}{\partial t} + (\mathbf{v} \cdot \nabla)(), \quad (36)$$

where \mathbf{v} is the local convection or advection speed. Considering the substantial derivative for the 1-D case, ϕ_t can be computed with the known boundary motion,

$$\phi_t = \ddot{x}_b - \dot{x}_b \phi_x. \quad (37)$$

Since ϕ_t and ϕ_x are not known on the boundary, additional Taylor series expansions for these terms need to be utilized. Considering the Taylor series expansions for ϕ_t and ϕ_x in Equation 37, $\phi_{t,i}^{n_\tau}$ can be eliminated from Equation 35, and the final equation reads as follows:

$$\begin{aligned} \dot{x}_b - \Delta t \ddot{x}_b = & \phi_i^{n_\tau} + (\Delta x - \dot{x}_b \Delta t) \phi_{x,i}^{n_\tau} - \frac{\Delta t^2}{2!} \phi_{tt,i}^{n_\tau} - \dot{x}_b \Delta t^2 \phi_{xt,i}^{n_\tau} + \\ & \left(\frac{\Delta x^2}{2!} - \dot{x}_b \Delta t \Delta x \right) \phi_{xx,i}^{n_\tau} + \mathcal{O}(\Delta x^3, \Delta t^3). \end{aligned} \quad (38)$$

Depending on the desired order of approximations in space and time, the above Equation 38 may need to be considered at different boundary points for different instances in time. For the 1-D case, the solid-fluid interface is only represented by one Lagrangian marker point, and therefore, five different time-levels need to be considered so that $\phi_i^{n_\tau}$ can be approximated to $\mathcal{O}(\Delta x^3, \Delta t^3)$. In the 2-D case, only three different time-levels need to be considered to achieve second-order accuracy in time. However, due to the increased dimension in space, additional Lagrangian marker points on the moving boundary have to be included. Finally, a linear system of nine equations has to be solved to determine the nine unknowns in the 2-D case (see for example Brehm and Fasel [7]). Once the system of equations is solved, an approximation for $\phi_i^{n_\tau}$ and $\phi_{x,i}^{n_\tau}$ is obtained. To approximate the second derivative of ϕ , $\phi_{xx,i}^{n_\tau}$, the continuous equation can be evaluated at (τ, x_i) ,

$$u_{t,i}^{n_\tau} = -u_i^{n_\tau} u_{x,i}^{n_\tau} + \mu u_{xx,i}^{n_\tau} = \ddot{x}_b^{n_\tau} - \dot{x}_b^{n_\tau} u_{x,i}^{n_\tau} \longrightarrow \mu u_{xx,i}^{n_\tau} = \ddot{x}_b^{n_\tau}. \quad (39)$$

At this point, all unknowns are determined and by considering Equation 34, one can solve for u_i at the next time-step t_{n+1} .

Regarding the second approach, instead of developing the Taylor series expansions about (τ, x_i) , it is reasonable to immediately approximate ϕ_i at the next time-step t_{n+1} , which eliminates the evaluation of the governing equations at this point. When the boundary motion is known *a priori*, this strategy presents a viable path as demonstrated by the validation results. For strongly coupled FSI applications, the second approach needs to be explored from a numerical stability point-of-view, because the coupling of the boundary motion with the fluid motion provides an additional challenge when the boundary location, velocity, and acceleration are not known *a priori*. The methodology on how to obtain the pressure at the “freshly-cleared”

grid point for the incompressible Navier-Stokes equations by approximating the pressure gradient at the “freshly-cleared” grid point is outlined in Brehm and Fasel [7].

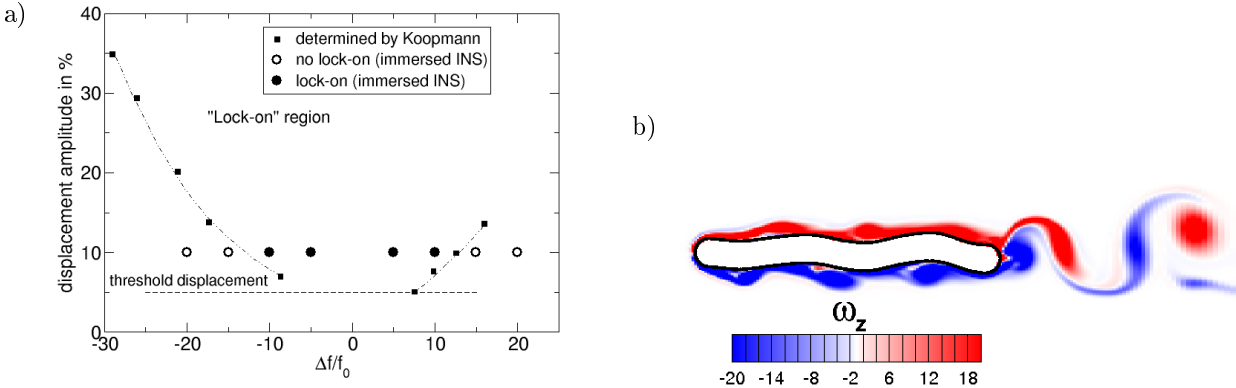


Figure 19: *a)* Comparison of “lock-on” for transversely oscillating cylinder and *b)* contours of streamwise vorticity for flow past a flexible filament.

The moving boundary capabilities, as briefly presented in this paper, were validated in Brehm and Fasel [7] by reproducing the vortex shedding lock-on, which is associated with a transversely oscillating cylinder. The results obtained compared well to the experimental data by Koopmann [25] and the computational results by Udaykumar et al. [40] for a cylinder oscillation amplitude of $A = 10\%D$ (shown in Figure 19a). As an example of a fully coupled FSI problem, the flow past a flexible filament was investigated (Figure 19b). A strong interaction between the filament and the flow dynamics was observed. By varying the properties of the filament, such as rigidity and mass per unit length, it was possible to excite different mode shapes in the structure. For particular parameter values, including the Reynolds number of the flow field, a resonance between the dynamics of the structure and the flow field was generated. In this situation, large deformations of the structure were observed and the flow field was dominated by the resonance frequency and its higher harmonics. The results demonstrate that the current method is applicable for other FSI applications, such as deforming, plunging airplane wings or for bio-fluid dynamics applications. The application of the immersed method to moving boundary problems concludes the discussion on possible extensions of the immersed method to different types of equations. The above demonstrates that the general strategy of locally enhancing the stability of the immersed boundary method can be applied to various types of equations, which are of great interest for problems in engineering and science.

4 Conclusions

The current paper has outlined a general approach for enhancing the stability properties of immersed boundary methods. It must be emphasized that immersed boundary methods are commonly derived solely by considering the accuracy of the numerical scheme. The stability properties are then commonly investigated afterwards. The unique feature of the presented immersed boundary approach is that in addition to a system of equation in terms of the stencil coefficients determining the accuracy of the numerical scheme, local stability constraints are considered in the derivation. One key finding of this research is that it is indeed possible to improve the spectral properties of the overall finite-difference scheme with immersed boundary treatment by locally adjusting the stencil coefficients at the irregular grid points instead of solving a large N -dimensional optimization problem (assuming N irregular grid points). The method has been applied to the incompressible Navier-Stokes equations including fluid-structure-interaction, and the compressible Navier-Stokes equations, as well as Maxwell’s equations with material interfaces. The presented stability analyses and error convergence studies demonstrate the full functionality and improved stability of the presented immersed boundary method.

5 Acknowledgments

This work was funded by the by the Air Force Office of Scientific Research (AFOSR) under grant number FA9550-09-1-0214 with Douglas R. Smith as the program manager and it was completed by the first author during his graduate studies at the University of Arizona.

References

- [1] A. Brandt. Multilevel Adaptive Solutions to Boundary-Value Problems. *Math. Comp.*, 31:311–332, 1977.
- [2] Achi Brandt. Guide to multigrid development. In W. Hackbusch and U. Trottenberg, editors, *Multigrid Methods*, volume 960 of *Lecture Notes in Mathematics*, pages 220–312. Springer Berlin / Heidelberg, 1982. 10.1007/BFb0069930.
- [3] C. Brehm and H. F. Fasel. A Non-Staggered Immersed Interface Method for Solving the Incompressible Navier–Stokes Equations. *40th Fluid Dynamics Conference and Exhibit, AIAA–2010–4433*, 2010.
- [4] C. Brehm and H. F. Fasel. Novel Immersed Interface Method Based on Local Stability Condition. *40th Fluid Dynamics Conference and Exhibit, AIAA–2010–4432*, 2010.
- [5] C. Brehm and H. F. Fasel. A Novel Concept for the Design of Immersed Boundary/Interface Methods. *Journal of Computational Physics, submitted*, 2011.
- [6] C. Brehm and H. F. Fasel. BiGlobal Stability Analysis as an Initial Value Problem for a Stalled Airfoil. *41st AIAA Fluid Dynamics Conference and Exhibit, AIAA–2011–3569*, 2011.
- [7] C. Brehm and H. F. Fasel. Immersed Interface Method for Solving the Incompressible Navier–Stokes Equations with Moving Boundaries. *49th AIAA Aerospace Sciences Meeting, AIAA–2011–0758*, 2011.
- [8] C. Brehm and H. F. Fasel. Stability Investigation of Axisymmetric Stenotic Flows. *41st AIAA Fluid Dynamics Conference and Exhibit, AIAA–2011–3272*, 2011.
- [9] C. Brehm, C. Hader, and H. F. Fasel. Novel Immersed Boundary/Interface Method for the Compressible Navier–Stokes Equations. *AIAA 2012–1110*, 2012.
- [10] C. Brehm, C. Koevary, T. Dackermann, and H. F. Fasel. Numerical Investigations of the Influence of Distributed Roughness on Blasius Boundary Layer Stability. *49th AIAA Aerospace Sciences Meeting, AIAA–2011–0563*, 2011.
- [11] G. Brès, T. Colonius, and A. V. Fedorov. Stability of Temporally Evolving Supersonic Boundary Layers over Micro-Cavities for Ultrasonic Absorptive Coatings. *AIAA 2008-4337*, 2008.
- [12] W. L. Briggs. *A Multigrid Tutorial*. Philadelphia, PA: SIAM, 1987.
- [13] D. L. Brown, R. Cortez, and M. L. Minion. Accurate Projection Methods for the Incompressible Navier–Stokes Equations. *Journal of Computational Physics*, 168:464–499, 2001.
- [14] P. G. Ciarlet. Discrete Maximum Principle for Finite-Difference Operators. *Aequations Math.*, 4:338–352, 1970.
- [15] A. V. Fedorov. Temporal Stability of Hypersonic Boundary Layer on Porous Wall: Comparison of Theory with DNS. *AIAA 2010-1242*, 2010.
- [16] A. V. Fedorov, V. Kozlov, A. Shpiyuk, A. Maslov, and N. D. Malmuth. Stability of Hypersonic Boundary Layer on Porous Wall with Regular Microstructure. *AIAA Journal*, 44(8):1866–1871, August 2006.
- [17] A. V. Fedorov, N. D. Malmuth, A. Rasheed, and H. G. Hornung. Stabilization of Hypersonic Boundary Layers by Porous Coatings. *AIAA Journal*, 39(4), 2001.
- [18] J. Ferziger and M. Peric. *Computational Methods in Fluid Dynamics*. New York: Springer–Verlag, 1996.
- [19] M. Gaster. The Influence of Surface Roughness on Boundary Layer Instability. *AFOSR Review meeting, Dallas*, 2008.
- [20] R. D. Guy and L. F. Fogelson. Stability of Approximate Projection Method on Cell–Centered Grids. *J. Comput. Phys.*, 203(2):517–538, 2005.
- [21] W. Hackbusch. *Multigrid Methods and Applications*. Springer-Verlag, Berlin, 1985.
- [22] C. Hader and H. F. Fasel. Numerical Investigation of Porous Walls for a Mach 6.0 Boundary Layer Using an Immersed Boundary Method. *41st AIAA Fluid Dynamics Conference and Exhibit, AIAA–2011–3081*, 2011.

- [23] P. W. Hemker and P. M. de Zeeuw. Some Implementations of Multigrid Linear Solvers. *in: Multigrid Methods for Integral and Differential Equations, Clarendon Press*, pages 85–116, 1985.
- [24] J. Kim and P. Moin. Application of a Fractional-Step Method to Incompressible Navier–Stokes Equations. *Journal of Computational Physics*, 59:308–323, 1985.
- [25] G. H. Koopmann. The Vortex Wakes of Vibrating Cylinders at Low Reynolds Numbers. *J. Fluid Mech.*, 28:501–512, 1967.
- [26] A. C. Laible and H. F. Fasel. Temporal Direct Numerical Simulations of Oblique Breakdown for a Cone at Mach 3.5. *49th AIAA Aerospace Sciences Meeting, 2011–0209*, 2011.
- [27] Z. Li and K. Ito. *The Immersed Interface Method; Numerical Solutions of PDEs Involving Interfaces and Irregular Domains*. SIAM book, 2006.
- [28] M. Linnick and H. Fasel. A High-Order Immersed Interface Method for Simulating Unsteady Incompressible Flows on Irregular Domains. *J. Comput. Phys*, 204:157–192, 2004.
- [29] S. F. McCormick. *Multilevel Adaptive Methods for Partial Differential Equations*. Philadelphia, PA: SIAM, 1989.
- [30] L. H. Meitz and H. F. Fasel. A Compact-Difference Scheme for the Navier–Stokes Equations in Vorticity-Velocity Formulation. *J. Comput. Phys.*, 157:371–403, 2000.
- [31] R. Mittal and G. Iaccarino. Immersed Boundary Methods. *Annu. Rev. Fluid Mech.*, 37:239–261, 2005.
- [32] S. Moini-Yekta, M. Barad, E. Sozer, J. Hosman, C. Brehm, and C. Kiris. Towards Hybrid Grid Simulations of the Launch Environment. *Seventh International Conference on CFD, ICCFD7–3102*, 2012.
- [33] David Marshall Norman D. Malmuth, Alexander V. Fedorov. Ultrasonically Absorptive Coatings for Hypersonic Laminar Flow Control, 2008.
- [34] C. Peskin. Numerical Analysis of Blood Flow in the Heart. *J. Comput. Phys.*, 25:220–252, 1977.
- [35] C. S. Peskin. The Immersed Boundary Method. *Acta Numerica, Cambridge University Press*, pages 1–39, 2002.
- [36] M. M. Rai and P. Moin. Direct Simulations of Turbulent Flow Using Finite-Difference Schemes. *J. Comput. Phys*, 96:15–43, 1991.
- [37] N. D. Sandham and H. Lüdeke. A numerical study of Mach 6 boundary layer stabilization by means of a porous surface. *AIAA 2009-1288*, 2009.
- [38] Wessling P. Sonneveld, P. and P. M. de Zeeuw. Multigrid and Conjugate Gradient Methods as Convergence Acceleration Techniques. *in: Multigrid Methods for Integral and Differential Equations, Clarendon Press*, pages 117–167, 1985.
- [39] T. Tezduyar. Finite Element Methods for Flow Problems with Moving Boundaries and Interfaces. *Arch. Comput. Methods Eng.*, 8:83–130, 2001.
- [40] H. S. Udaykumar, R. Mittal, P. Rampunggoon, and A. Khanna. A Sharp Interface Cartesian Grid Method for Simulating Flows with Complex Moving Boundaries. *J. Comput. Phys.*, 174:345–380, 2001.
- [41] B. van Leer. Flux Splitting for the Euler Equations. *International Conference on Numerical Methods in Fluid Dynamics*, 170:507–512, 1982.
- [42] V. Wartemann, H. Lüdeke, and N. D. Sandham. Stability analysis of hypersonic boundary layer flow over microporous surfaces. *16th AIAA/DLR/DGLR International Space Planes and Hypersonic Systems and Technologies Conference*, 2010.
- [43] A. Wiegmann and K. Bube. The Explicit-Jump Immersed Interface Method: Finite Difference Methods for PDEs with Piecewise Smooth Solutions. *SIAM J. Numer. Anal.*, 31(4):1019–1044, 1992.
- [44] K. R. Yee. Numerical Solution of Initial Boundary Value Problems Involving Maxwell’s Equations in Isotropic Media. *IEEE Trans. on Antennas and Propagation*, AP-16:302–307, 1966.
- [45] P. M. De Zeeuw. Matrix-dependent prolongations and restrictions in a blackbox multigrid solver. *Journal of Computational and Applied Mathematics*, 33(1):1 – 27, 1990.
- [46] X. Zhong. High-Order Finite-Difference Schemes for Numerical Simulation of Hypersonic Boundary-Layer Transition. *J. Comp. Phys.*, 144:662–709, 1998.
- [47] X. Zhong. A New High-Order Immersed Interface Method for Solving Elliptic Equations with Embedded Interface of Discontinuity. *Journal of Computational Physics*, 225:1066–1099, 2007.